Supporting Information for the manuscript

Efficient hydrogen evolution reaction with platinum stannide $PtSn_4$ via surface oxidation

Danil W. Boukhvalov, Andrea Marchionni, Jonathan Filippi, Chia-Nung Kuo, Jun Fuji, Raju Edla, Silvia Nappini, Gianluca D'Olimpio, Luca Ottaviano, Chin Shan Lue, Piero Torelli, Francesco Vizza and Antonio Politano

S1. X-ray diffraction (XRD) analysis

The left panel of Figure S1 shows the XRD pattern of single crystals of (010)-oriented $PtSn_4$.

The right panel of the same Fig. reports the corresponding Laue diffraction.

The obtained lattice constants are a = (6.405±0.002) Å, b=(11.371±0.002) Å, c = (6.372±0.002) Å. These values are consistent with previous reports in literature [1].

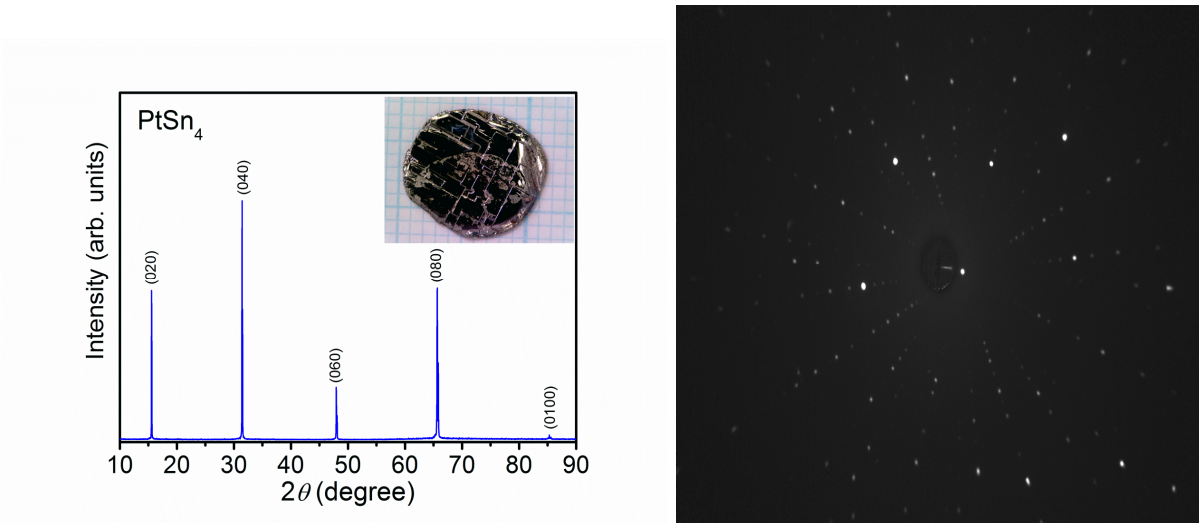

Figure S1. (left panel) Room-temperature single-crystal x-ray diffraction pattern from the (010) plane of $PtSn_4$. The inset shows a photograph of an as-grown $PtSn_4$ single crystal. (right panel) Laue diffraction image taken along the (010) direction.

S2. Survey XPS spectrum of $PtSn_4$

Survey XPS spectrum is reported in Fig. S2. Notably, no C-1s and O-1s are detected, thus ensuring surface cleanliness.

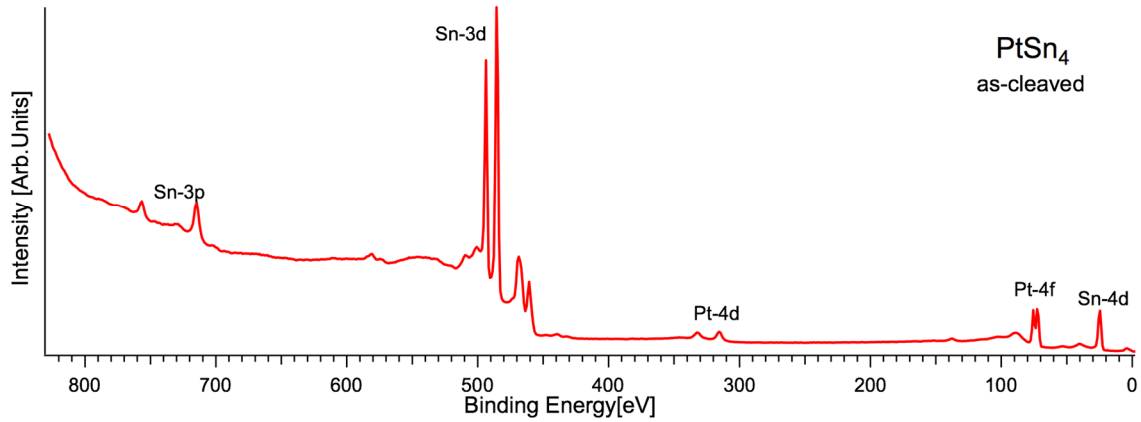

Figure S2. XPS survey scan of as-cleaved sample, clearly showing the cleanliness of the surface (especially, no C-1s and O-1s components). The photon energy is 800 eV.

S3. Compositional (Sn/Pt ratio) depth profile

To evaluate the compositional (Sn/Pt ratio) depth profile of $PtSn_4$, XPS experiments were performed at various photon energies (800, 400 and 300 eV) and, moreover, at various emission angles (65,55 and 45 degrees) with a photon energy of 400 eV. The energy dependent XPS analysis indicated an increased Sn/Pt ratio at decreasing photon energy, i.e. in conditions with higher surface sensitivity. Congruently, the angle-dependent photoemission revealed an increased ratio of Sn/Pt going from normal (90°) to grazing (45°) emission angle, i.e. in conditions with higher surface sensitivity. Therefore, both energy- and angle-dependent analysis indicate the occurrence of a Sn-terminated surface. The respective photon energy and angle-dependent values of the Sn/Pt ratio are reported in Table S1.

Table S1. Values of the Sn/Pt ratio obtained for an as-cleaved $PtSn_4$ sample evaluated by XPS spectra acquired using different (i) photon energy (800, 400 and 300 eV) and (ii) emission angles (65, 55 and 45 degrees)

Photon Energy	**Geometry**	**Sn/Pt ratio**
900 eV	Normal Emission	4.3±0.6
400 eV	Normal Emission	5.4±0.8
300 eV	Normal Emission	6.3±0.9
400 eV	90° Emission	4.3±0.7
400 eV	65° Emission	5.0±0.7
400 eV	55° Emission	5.7±0.8
400 eV	45° Emission	5.3±0.8

S4. O-1s core level

For both H_2O- and O_2-dosed $PtSn_4$, we find (Fig. S3) one O-1s main component at ~530.3 eV and minor components at 529.6 eV ascribable to the formation of SnO/Sn-OH and SnO species[2, 3], congruently with the corresponding component at ~486.2 eV[1] in the Sn-3d spectrum, and to Sn-O-Sn bonds arising in the early stages of tin-oxide formation [2, 4] respectively. A small component at a BE of ~531.5eV can be associated to the chemisorption of OH or H_2O species [5-7] in H_2O-exposed $PtSn_4$ surface. The O-1s region in the O_2-dosed sample also shows an additional component at 530.9 eV, which is ascribable to the formation of SnO_2 .[1] The same contribution is also observed in the corresponding Sn-3d core level spectrum in Fig. 3 of the main text, where the small component at 487.2 eV can be assigned to SnO_2 (5% of the total spectral area) [8]. It should be mentioned that a strong H_2O-induced band bending has been previously reported for water adsorption on SnO_2 [9], as a consequence of the formation of surface hydroxyls.

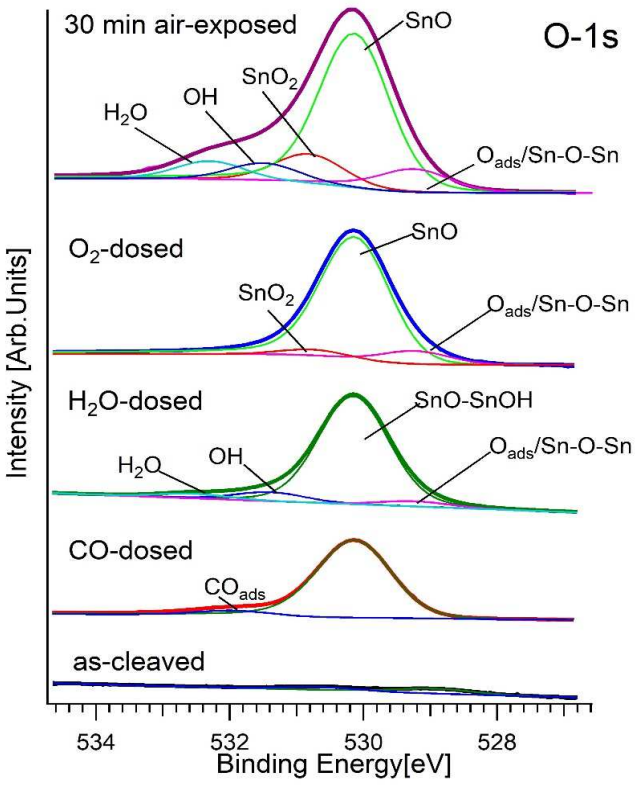

Figure S3. O-1s core-level spectra for as-cleaved, CO-dosed, H_2O-dosed, O_2-dosed and air-exposed (30 minutes) $PtSn_4$. The photon energy is 800 eV.

S5. Vibrational spectroscopy

To provide further evidence of CO tolerance of $PtSn_4$, we carried out a vibrational investigation by HREELS (Fig. S4), finding a featureless spectrum in the region of C-O stretching in the 210-255 meV range (see Ref. [10] for a review of vibrational investigations on CO/metals), thus confirming that $PtSn_4$ could represent a perfectly CO tolerant electrode, contrary to other Pt-based alloys (see the comparison with the case of Pt_3Ni in Supplementary Information, Section S7). For the sake of completeness, CO coverage can be estimated to be of the order ~10^{-3} ML by considering both HREELS results in Fig. S4 and O-1s in Fig. S3. Remarkably, the vibrational spectrum of the CO-dosed $PtSn_4$ surface is characterized by a feature at 60 meV accompanied by a weak peak at 120 meV, that are associated to the SnO optical phonon at 60

meV[3] and its first-order replica, consistently with dissociative CO adsorption at defect sites. The same features are present also for direct exposure to O_2. The negligible dependence on the amount of the CO dose indicates fast saturation of active sites, further supporting the occurrence of dissociation at defect sites.

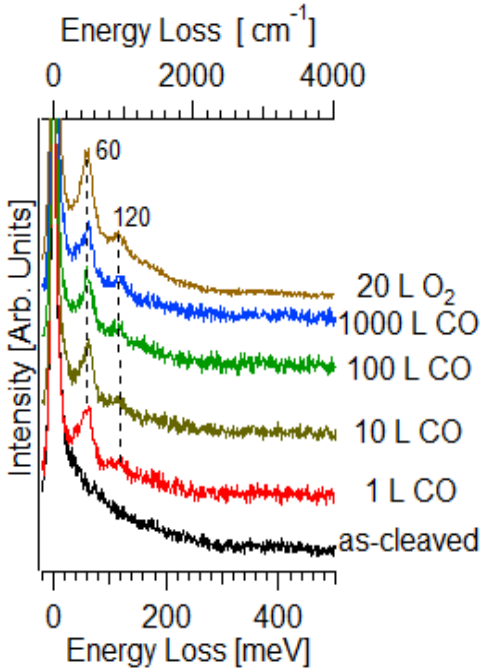

Figure S4. HREELS spectra for pristine $PtSn_4$ and the same surface modified by the exposure to different amounts (1-1000 L) of CO and to 20 L of O_2 at room temperature. The impinging energy is 4 eV. All spectra were normalized to the intensity of the elastic peak and recorded in specular direction, with an incidence angle of 55° with respect to the sample normal.

S6. Valence band

The eventual effects of chemisorption and oxidation on electronic properties were assessed by measuring the valence band (Fig. S5), finding that surface treatments and air exposure only produced minimal effects. Being topological properties connected to Dirac node arcs located in the nearness of the Fermi level [11], it is evident that this finding is consistent with the robustness of the topological states of the bulk crystal of $PtSn_4$, which are not modified by the presence of the tin-oxide skin. However, Dirac node arcs are expected to be quenched,

since they arise from dangling bonds in the surface layer, which are not present in the tin-oxide skin.

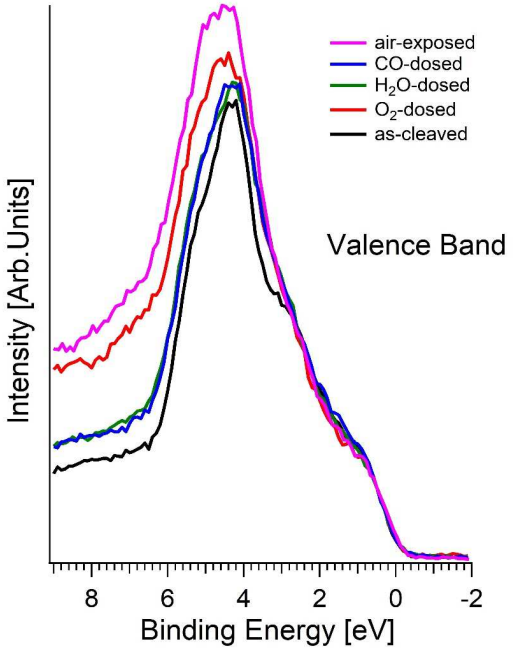

Figure S5. Valence-band spectra normalized to the Fermi edge for as-cleaved, CO-dosed, H_2O-dosed, O_2-dosed and air-exposed $PtSn_4$. The photon energy is 800 eV.

S7. Comparison with CO/Pt-skin $Pt_3Ni(111)$

The top panel of Fig. S6 shows the O-1s core level of CO-saturated Pt-skin of $Pt_3Ni(111)$. The observed value of the binding energy is consistent with CO adsorption on top sites at room temperature. The difference with O-1s in CO-dosed $PtSn_4$ (Fig. S3) is manifest. To gain more insights on the differences between $PtSn_4$ (Fig. S4) with Pt-skin-terminated $Pt_3Ni(111)$ and Pt(111) concerning the interaction with CO at room temperature, we carried out vibrational investigations by saturating the $Pt_3Ni(111)$ and Pt(111) surfaces at room temperature by an exposure of 10 L of CO (bottom panel of Fig. S6). No appreciable differences between the results attained for the $Pt_3Ni(111)$ and Pt(111) surfaces exist, while the case of $PtSn_4(010)$ is

well different (see Fig. S4). The loss feature at 56 meV in the bottom panel of Fig. S6 is due to the vibration of the whole CO molecule against the Pt surface. Vibrational peaks at 230 and 258 meV arise from the intramolecular stretching vibration of CO adsorbed at bridge and atop sites, respectively, in agreement with previous results for CO adsorption on Pt(111) and other transition-metal systems [10].

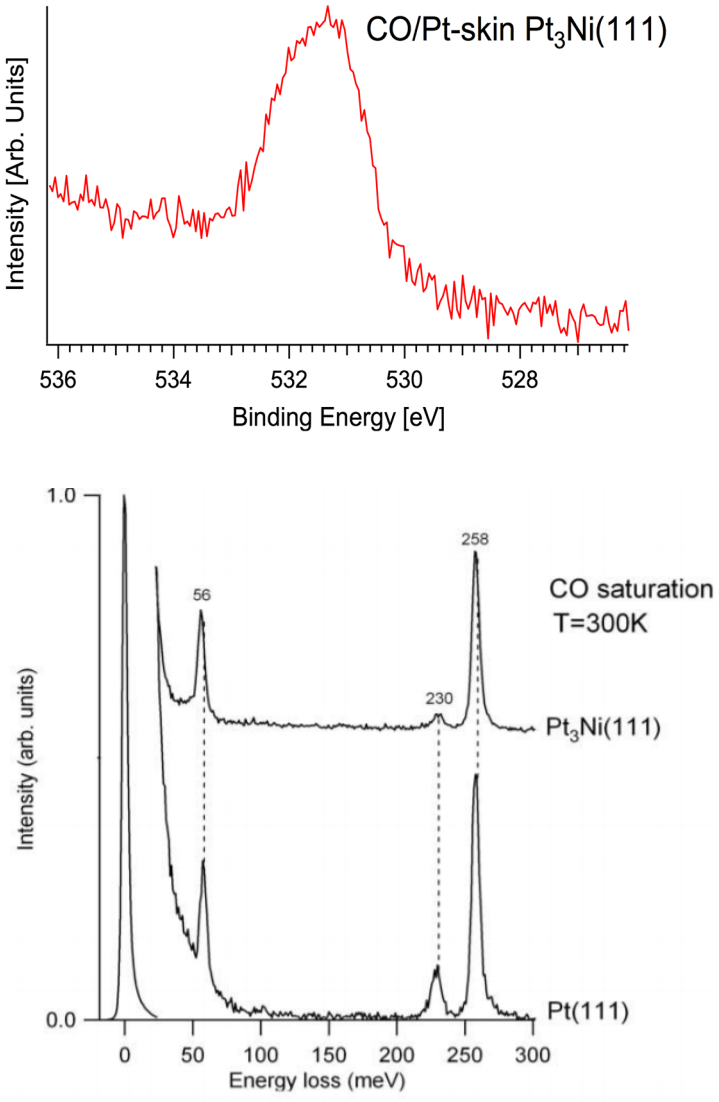

Figure S6. (top panel) O-1s core level for CO-exposed Pt-skin-terminated $Pt_3Ni(111)$. Photon energy is 650 eV. This spectrum has been acquired at the SuperESCA beamline at Elettra synchrotron, Trieste. Differences compared to the case of CO-exposed $PtSn_4$ in Fig. S3 are evident. (bottom panel) HREELS spectra for the CO-saturated Pt(111) and $Pt_3Ni(111)$ surfaces. Both measurements and exposures have been carried out at 300 K. Spectra have been recorded in specular geometry (incidence angle 55° with respect to the sample normal) and with a primary electron beam energy of 4 eV.

S8. Sketch of atomic structures used for theoretical modelling

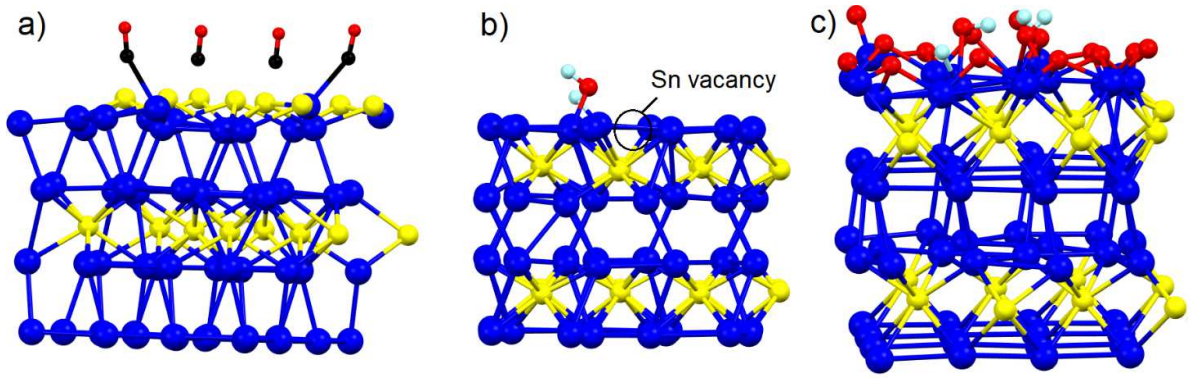

Figure S7. Optimized atomic structure of (a) the physisorption of CO molecules on Pt-terminated surface at saturation coverage and (b) decomposition of water molecule on 1Sn-terminated surface with one Sn vacancy and (c) four hydrogen atoms adsorbed on oxidized 1Sn-terminated surface (Volmer step of HER).

S9. HER and OER on pure and oxidized surfaces of $PtSn_4$

Firstly, in our model we checked the standard pathway of HER, i.e. (i) Volmer ($H^+ + e^- \rightarrow H_{ads}$) and, successively, (ii) Heyrovsky ($H_{ads} + H^+ + e^- \rightarrow H_2$) reactions. Calculations demonstrate rather high energy cost of Heyrovsky reaction (Fig. S8a), in contrast with experimental results. Therefore, we considered another opportunity: combination of (i) Volmer and (ii) Tafel steps (see main text).

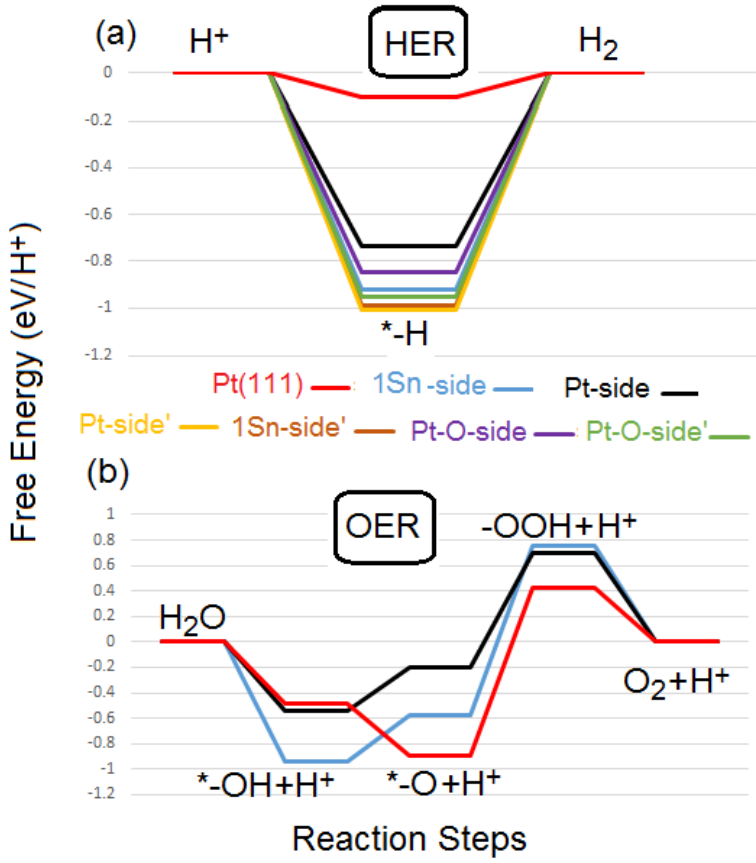

Figure S8. Free energy diagrams for hydrogen (a) and oxygen (b) evolution reactions on various surfaces of $PtSn_4$. The data for Pt(111) are adopted from the Ref. [12] Results for whole hydrogen coverage of Pt-terminated surface are marked by a prime symbol (').

S10. Electrochemical tests

Notably, similarity in HER with the case of Pt only appears whenever the $PtSn_4$ surface is exposed to potential higher than 1.035 V vs RHE. To elucidate this unexpected behavior, we reported (Fig. S9a) the current density of the backwards scan (from 0.05 to -0.05 V vs RHE) of the stable cycle as a function of the upper inversion potential value. The lower inversion potential remained the same for all these measurements (-0.1 V vs RHE). Thus, a strong dependence of HER activity with the upper inversion potential is manifest. By increasing the upper inversion potential (Fig. S9b), the absolute value of the current density at -50 mV vs RHE increases. Likewise, the current density during the forwards scan, related to the

hydrogen oxidation reaction (HOR), measured at -20 mV, exhibits the same trend.

By inspecting the behavior of the derivative of the current density at -50 mV as a function of the upper potential, it is evident that $PtSn_4$ behaves similarly to the Pt foil from 1.035 V as upper inversion potential. Increasing the upper potential limit, the current density still grows but with a lower slope. This suggests the key role of surface phenomena in HER promotion, starting around 1.0-1.1 V vs RHE, involving surface tin-oxide phases. To verify this phenomenon, we measured the Tafel slope for pristine sample and after a treatment at 1.035 V. As reported in Fig. S10, the slopes resulted to be 442 and 86 mV dec^{1}, respectively, thus confirming the improvement of HER kinetics after oxidation, in good agreement with theoretical findings.

However, we observed that performances of HER activity strikingly depend on surface preparation and treatments.

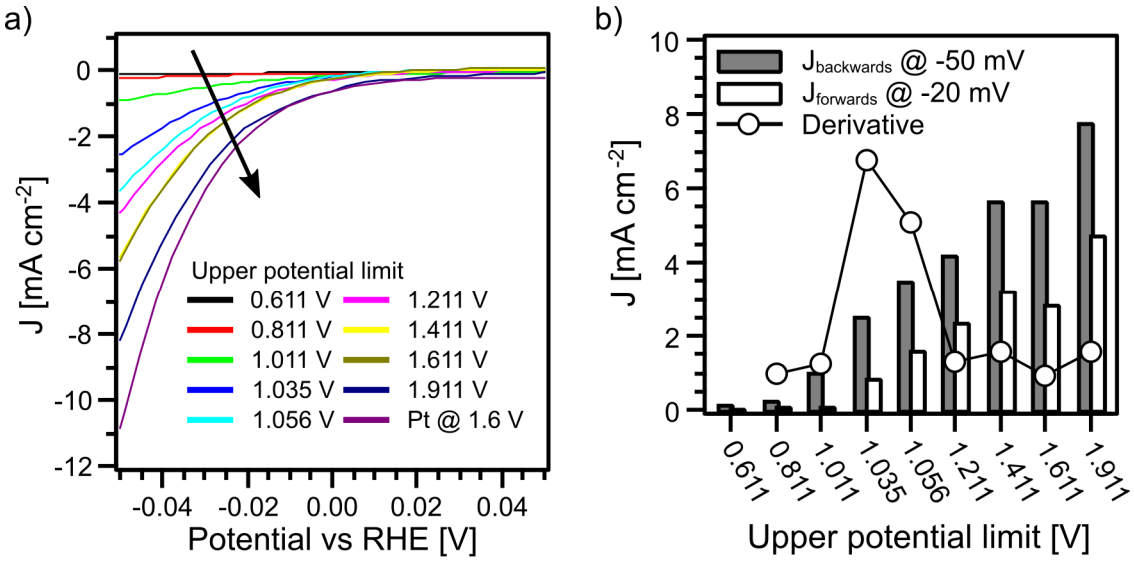

Figure S9. (a) Current density during the backwards scan (at 50 mV s^{-1}) as a function of the upper inversion potential limit. (b) Current density of the backwards scan at -50 mV (gray bars) and current density of the forwards scan at -20 mV (white bars). The derivative of the current density of the backwards scan at -50 mV is reported as white circles.

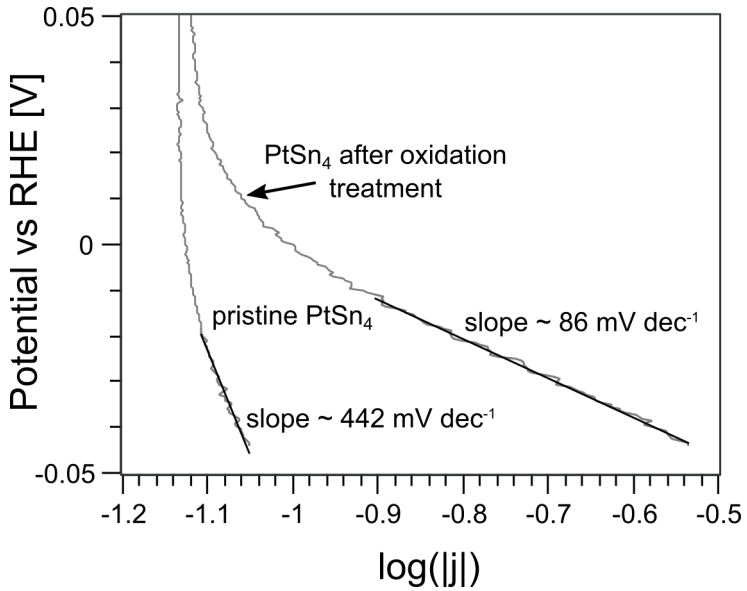

Figure S10. Tafel plot of pristine $PtSn_4$ and after the treatment at 1.035 V vs RHE registered at 1 mV s^{-1}.

Finally, Fig. S11 reports the results of the chronomaperometric experiment at -44 mV vs RHE for 12 hours in 0.05 M H_2SO_4, while Fig. S12 shows the chronoamperometric experiment at the potential of 1.8V vs RHE in 0.05M H_2SO_4 to test the durability of $PtSn_4$ towards OER.

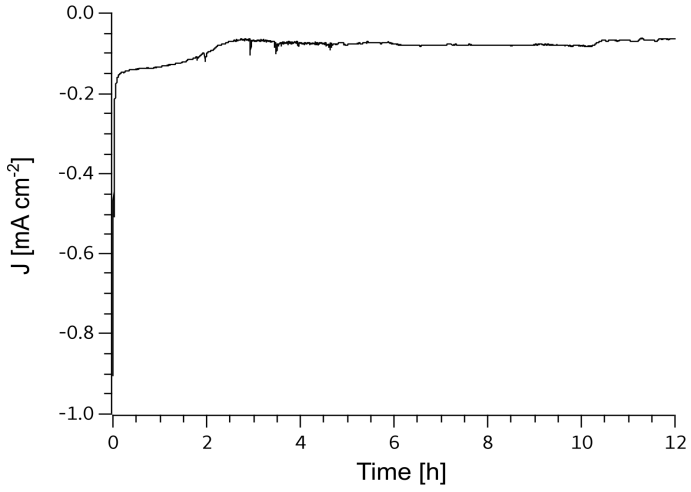

Figure S11. Chronomaperometric experiment at -44 mV vs RHE for 12 hours in 0.05 M H_2SO_4.

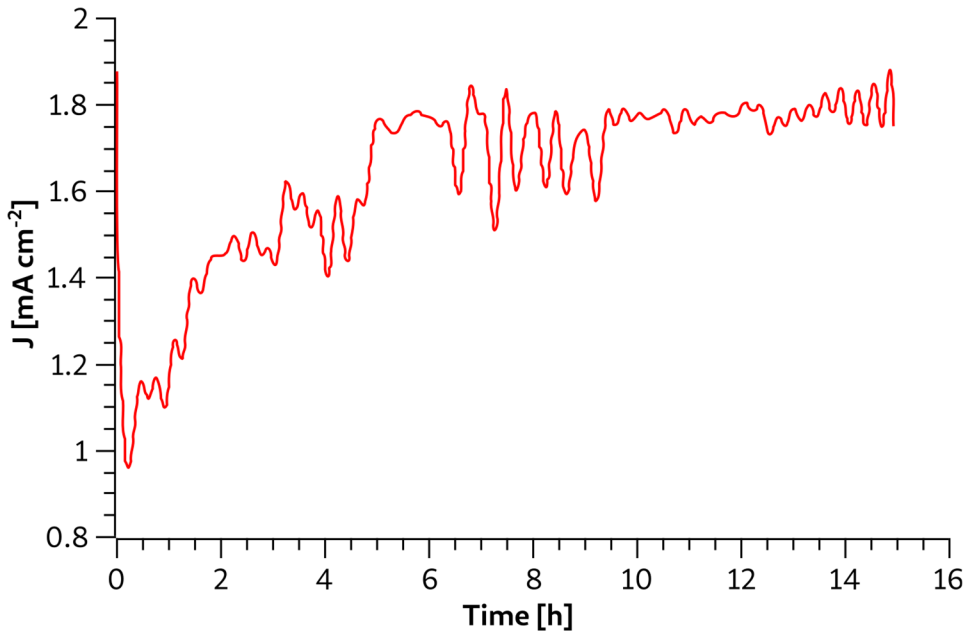

S12. Chronoamperometric experiment at the potential of 1.8V vs RHE in 0.05M H_2SO_4 to test the durability of $PtSn_4$ towards OER.

The impact of electrochemical treatment on surface morphology was addressed by SEM on the zones depicted in Fig. S13. SEM figures are shown in Figs. S14-S20.

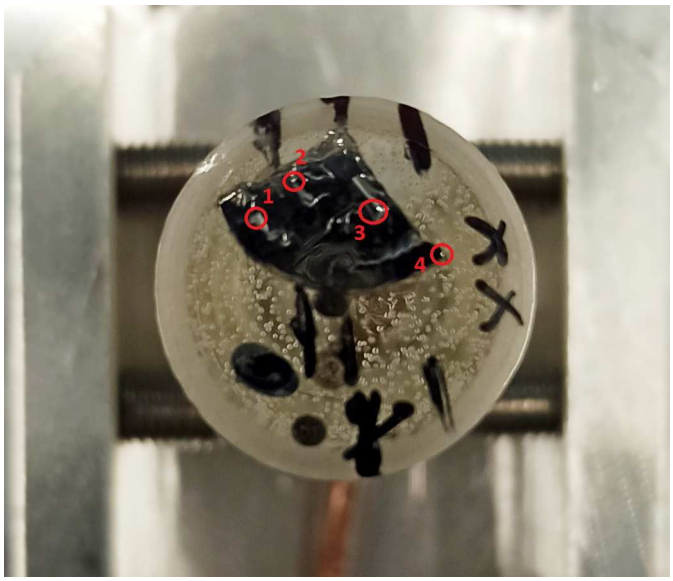

S13. Image of electrode with approx. area characterized by SEM. The electrode was masked the area in four parts, to be preserved by the electrochemical treatment. The first zone (1) was pristine, the second zone was treatment between -0.15 to 0.7 V (20 mV s^{-1}, 20 cycles), the third zone between -0.15 to 1.2 V (20 mV s^{-1}, 20 cycles), and the fourth between -0.15 to 1.8 V V (20 mV s^{-1}, 20 cycles).

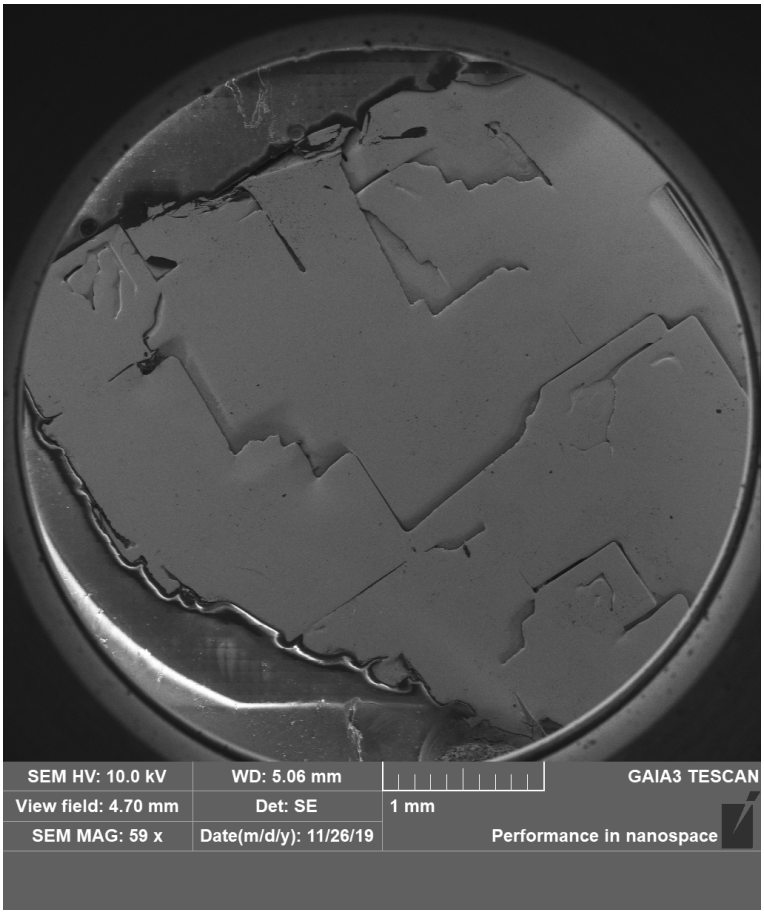

S14. Overall picture of the electrode by secondary electrons. Are visible only some terraces.

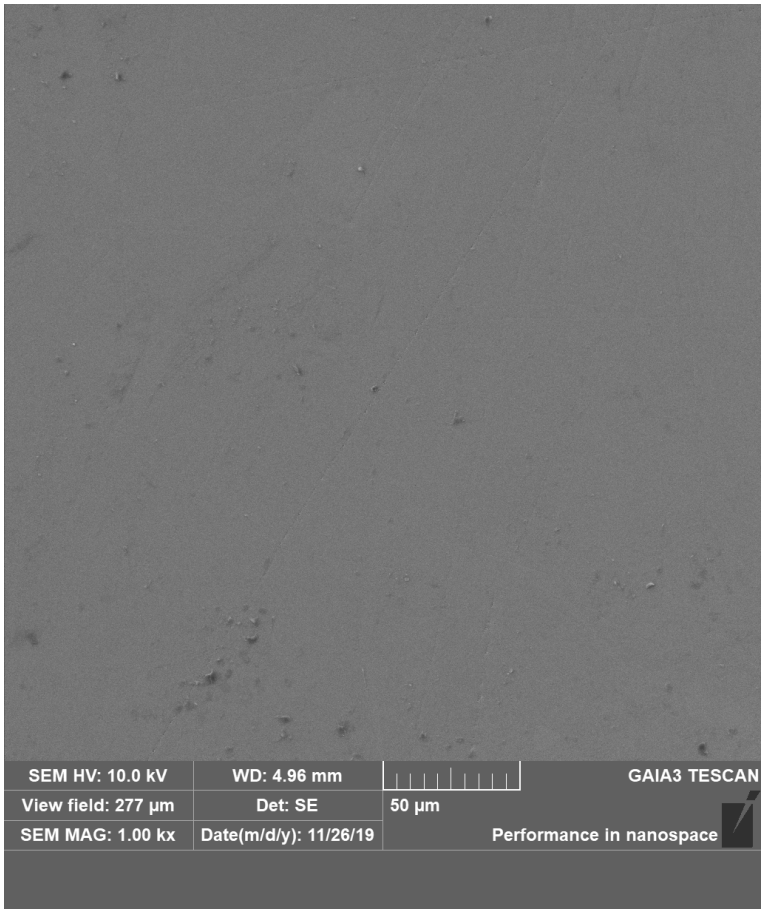

S15. Secondary electrons picture in the zone 1. Only some traces due by polishing treatment are visible.

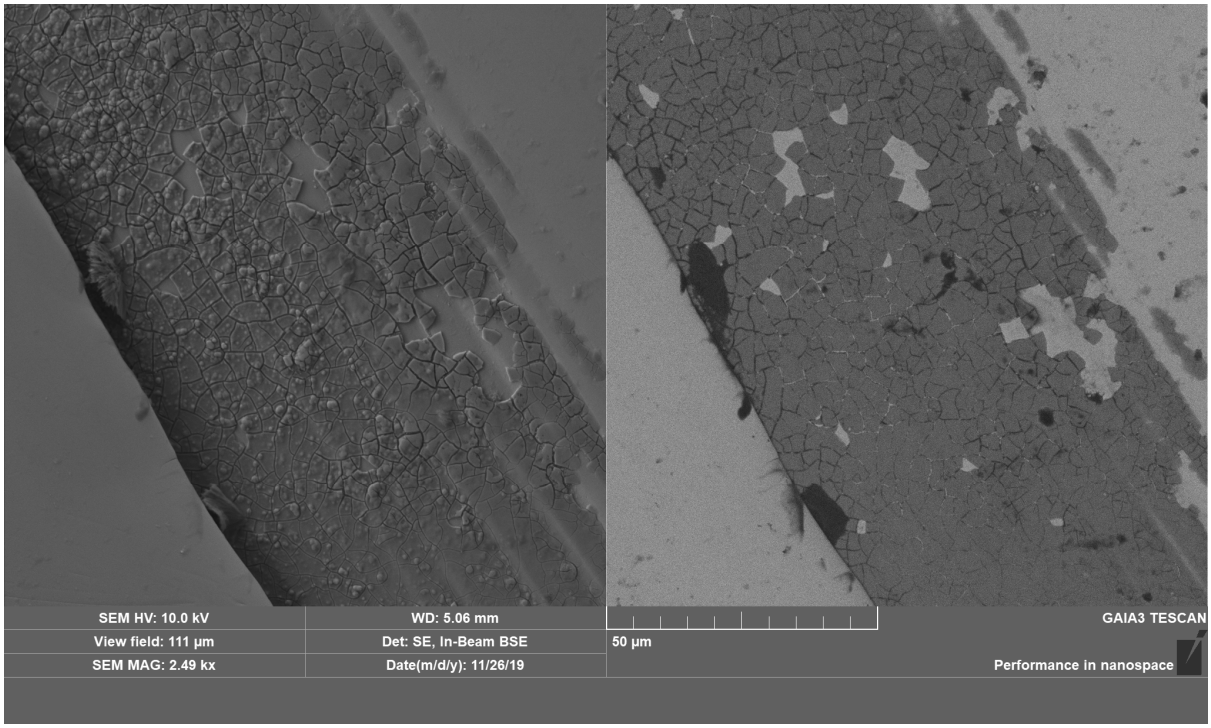

S16. Secondary and backscattered electrons picture in the zone 1. In a creek is visible a

cracked layer made by a lower density phase, probably due by oxidized species.

Furthermore, it is clear that this layer disappears near exposed and polished surfaces.

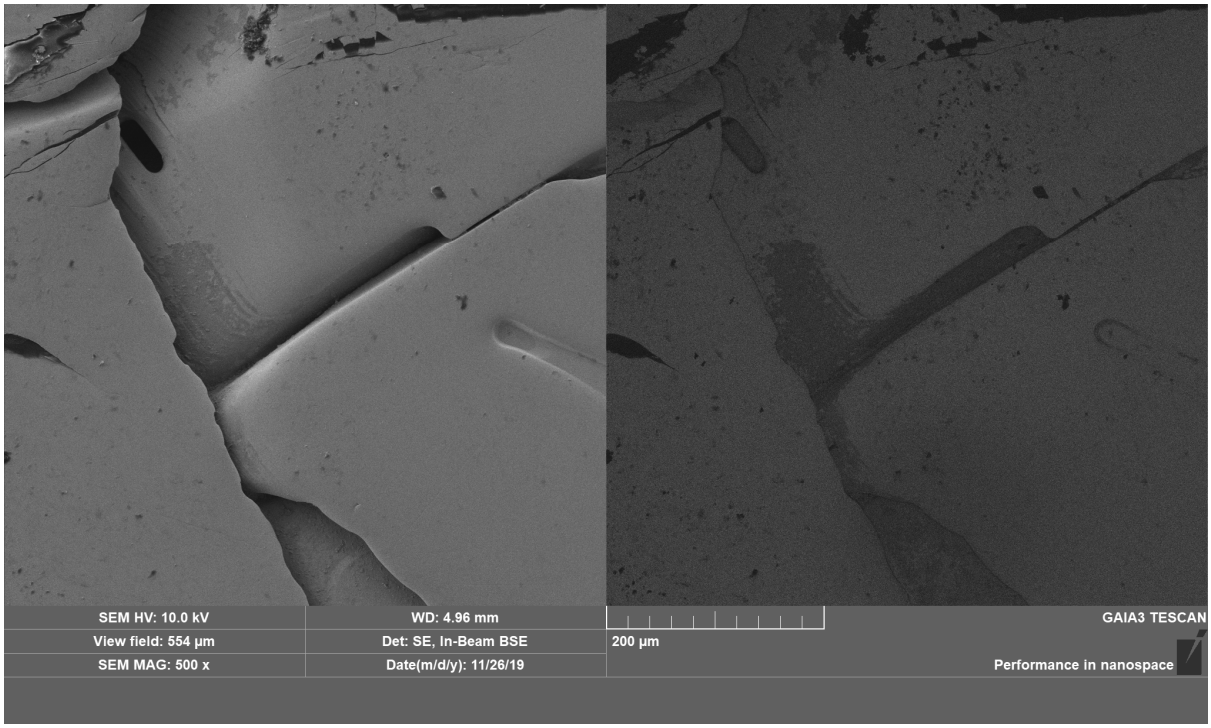

S17. Secondary and backscattered electrons image at low zoom in zone 2. Large polished surfaces have some creeks in which a lower density layer exists (in the center of area).

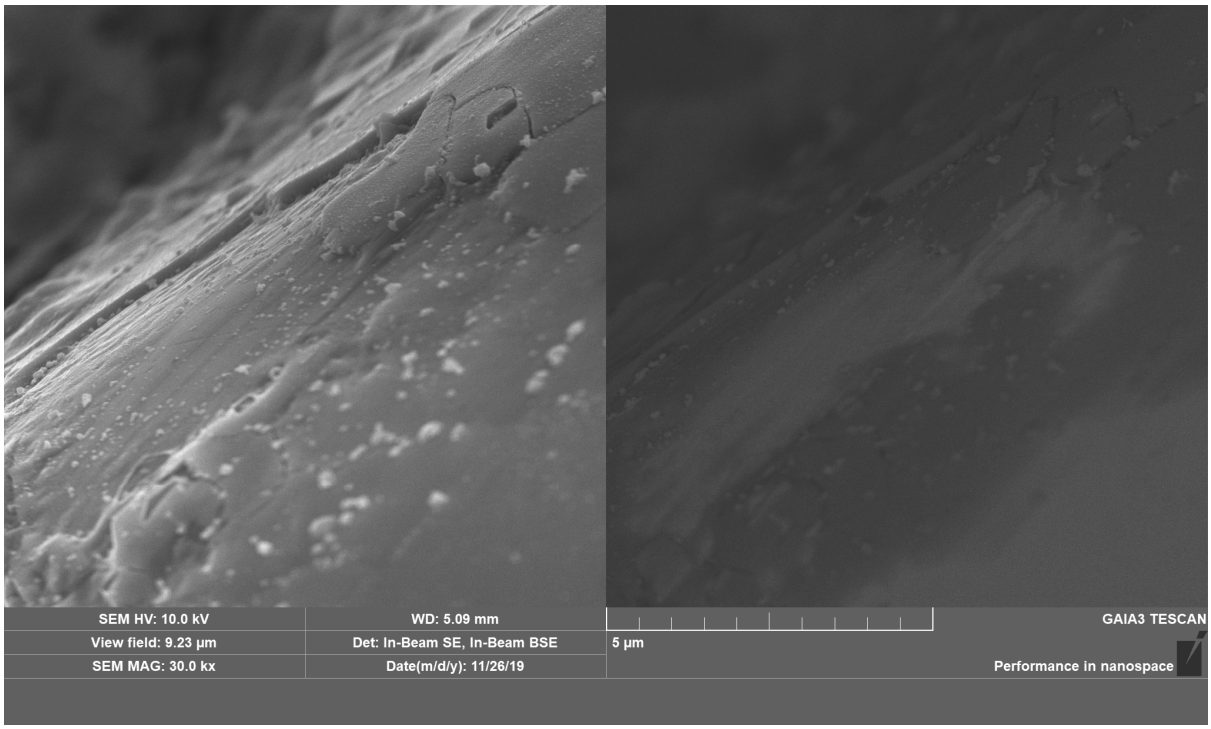

S18. Secondary and backscattered electrons image at high zoom in zone 2. On the edge of the

creek is visible a layer with lower density than the underlying surface. This is consistent with a shallow layer of oxide species.

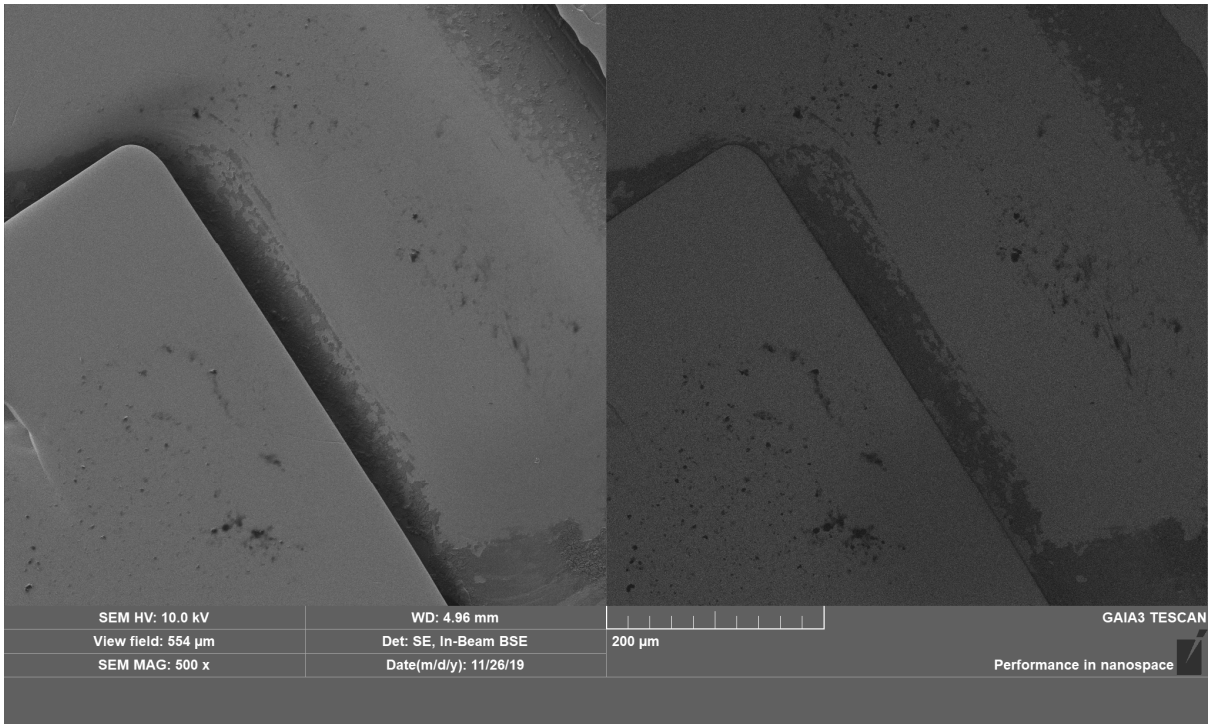

S19. Secondary and backscattered electrons image at high zoom in zone 3.

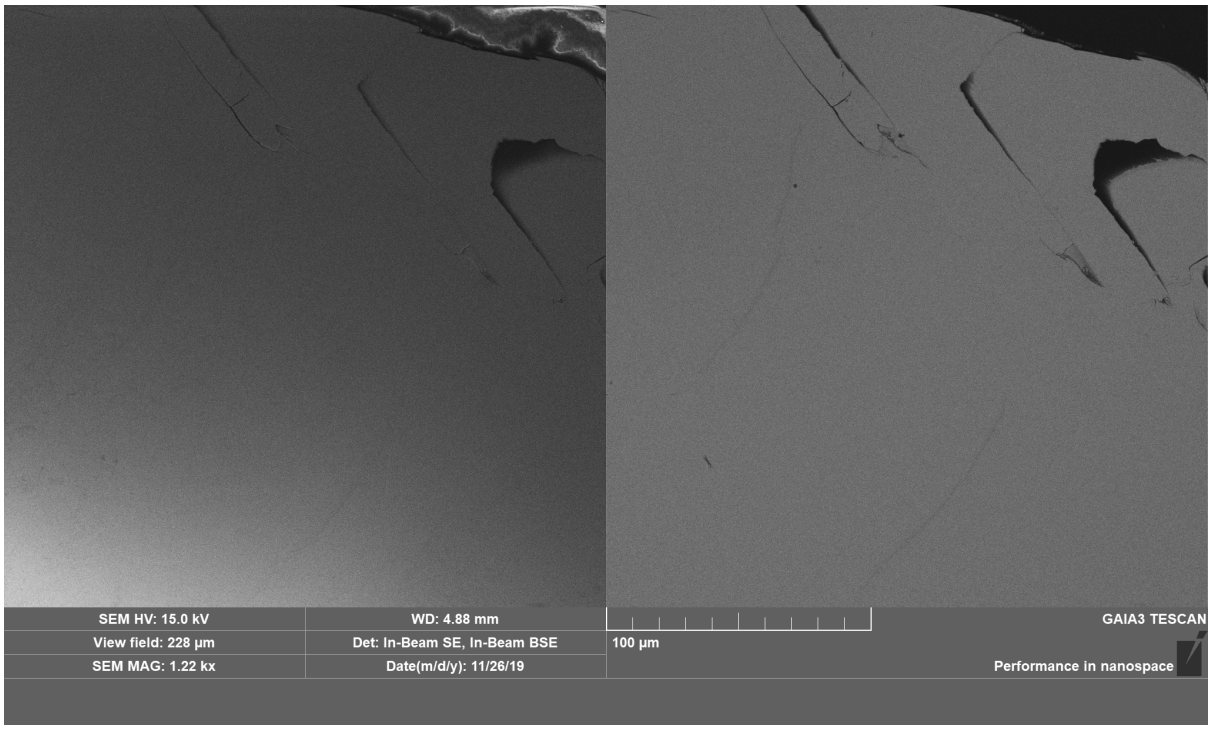

S20. Secondary and backscattered electrons image at low zoom in zone 4. We do not observe any inhomogeneous density on the exposed surface also after very oxidizing electrochemical

treatment.

S11 Fit procedures for XPS data

To evaluate binding energies (BEs) of core levels, a Shirley background was subtracted from raw XPS data. Pt-4f and Sn-3d core-level spectra were analyzed by using a Doniach–Sunjic function [13], convoluted with a Gaussian line-shape to account for experimental resolution, inhomogeneity, and temperature-derived broadening. Conversely, for O-1s core level we adopted Voigt line-shapes.

S12 Comparison with recent literature data

Catalyst	Electrolyte	Overpotential	Tafel slope (mV dec^{-1})	Ref.
$PtSn_4$ (foil)	0.05M H_2SO_4	25 mV @ 3 mA cm^{-2}	86	This work
Pt (foil)	0.05M H_2SO_4	22 mV @ 3 mA cm^{-2}	34	This work
Pt1Cu1.1/NPC (nanoparticles)	0.5M H_2SO_4	13 mV @ 10 mA cm^{-2}	34	10.1016/j.jcis.2019.10.062
Pt/C (nanoparticles)	0.5M H_2SO_4	20 mV @ 10 mA cm^{-2}	44	10.1016/j.jcis.2019.10.062
Pt/NPC (nanoparticles)	0.5M H_2SO_4	34 mV @ 10 mA cm^{-2}	37	10.1016/j.jcis.2019.10.062
PtRu@RFCS	0.5M H_2SO_4	19 mV @ 10 mA cm^{-2}	27	Energy Environ. Sci., 2018, 11, 1232-1239

PtCoFe@CN	0.5M H_2SO_4	45 @ 10 mA cm^{-2}	32	Energy Environ. Sci., 2013, 6, 1509-1512
Pt NC/rGO	0.5M H_2SO_4	54 @ 10 mA cm^{-2}	30	Nanoscale, 2017, 9, 10138-10144
Pd/Cu-Pt	0.5M H_2SO_4	23 @ 10 mA cm^{-2}	25	Angew. Chem. Int. Ed., 2017, 56, 16047-16051
Pt-MoO3−x NFs | MoS2	0.5M H_2SO_4	69 @ 10 mA cm^{-2}	53	https://doi.org/10.1016/j.jcat.2019.10.027
Ni@Pt/NNPC	0.5 M H_2SO_4	76 @ 20 mA cm^{-2}	46	https://doi.org/10.1016/j.electacta.2019.134895
Rh@NPCP	0.5 M H_2SO_4	20 @ 10 mA cm^{-2}	39	https://doi.org/10.1016/j.electacta.2019.134982

References

[1] B. Künnen, D. Niepmann, W. Jeitschko, *J. Alloys Compd.* **2000**, *309*, 1.

[2] Y. Jugnet, D. Loffreda, C. l. Dupont, F. o. Delbecq, E. Ehret, F. J. Cadete Santos Aires, B. S. Mun, F. Aksoy Akgul, Z. Liu, *J. Phys. Chem. Lett.* **2012**, *3*, 3707.

[3] W. Wan, Y. Ge, Y. Liu, *Appl. Phys. Lett.* **2019**, *114*, 031901.

[4] Z. Luo, J. Lu, C. Flox, R. Nafria, A. Genç, J. Arbiol, J. Llorca, M. Ibáñez, J. R. Morante, A. Cabot, *J. Mater. Chem. A* **2016**, *4*, 16706.

[5] P. R. Kidambi, B. C. Bayer, R. Blume, Z.-J. Wang, C. Baehtz, R. S. Weatherup, M.-G. Willinger, R. Schloegl, S. Hofmann, *Nano Lett.* **2013**, *13*, 4769.

[6] L.-Å. Näslund, *J. Chem. Phys.* **2014**, *140*, 104701.

[7] T. Schiros, L.-Å. Näslund, K. Andersson, J. Gyllenpalm, G. Karlberg, M. Odelius, H. Ogasawara, L. G. Pettersson, A. Nilsson, *J. Phys. Chem. C* **2007**, *111*, 15003.

[8] L. Liu, M. An, P. Yang, J. Zhang, *Sci. Rep.* **2015**, *5*, 9055.

[9] M. Batzill, K. Katsiev, J. M. Burst, Y. Losovyj, W. Bergermayer, I. Tanaka, U. Diebold, *J. Phys. Chem. Solids* **2006**, *67*, 1923.

[10] A. Politano, G. Chiarello, *J. Phys. Chem. C* **2011**, *115*, 13541.

[11] Y. Wu, L.-L. Wang, E. Mun, D. D. Johnson, D. Mou, L. Huang, Y. Lee, S. L. Bud'ko, P. C. Canfield, A. Kaminski, *Nat. Phys.* **2016**, *12*, 667.

[12] J. Greeley, T. F. Jaramillo, J. Bonde, I. Chorkendorff, J. K. Nørskov, *Nat. Mater.* **2006**, *5*, 909.

[13] S. Doniach, M. Sunjic, *J. Phys. C* **1970**, *3*, 285.